Prospect for measuring two-dimensional van der Waals magnets by Electron Magnetic Chiral Dichroism

Dongsheng Song[1,2]*, Fengshan Zheng[2] and Rafal E. Dunin-Borkowski[2]

1. Information Materials and Intelligent Sensing Laboratory of Anhui Province, Key Laboratory of Structure and Functional Regulation of Hybrid Materials of Ministry of Education, Institutes of Physical Science and Information Technology, Anhui University, Hefei 230601, China

2. Ernst Ruska-Centre for Microscopy and Spectroscopy with Electrons and Peter Grünberg Institute, Forschungszentrum Jülich, 52425 Jülich, Germany

*Corresponding author: dsong@ahu.edu.cn

Abstract

Two-dimensional (2D) van der Waals magnets have drawn considerable attention in recent years triggered by the huge interest in novel magnetism and spintronic devices. Magnetic measurement of 2D van der Waals (vdW) magnets is crucial to understand the physical origin of magnetism in 2D limits. Therefore, advanced magnetic characterization techniques are highly required. However, only a limited number of such techniques are available due to the extremely small volume of 2D vdW magnets. Here, we introduce the electron magnetic chiral dichroism (EMCD) technique in transmission electron microscope (TEM) to measure 2D vdW crystals. In comparison with some other already-employed techniques in 2D magnets, EMCD is able to quantitatively measure magnetic parameters in three orthogonal directions at nanometer or even at atomic scale. We then perform EMCD simulations on several typical 2D vdW magnets with respect to the accelerating voltage, the number of atomic layers and beam tilt under zone axial orientation. The intensity and distribution of EMCD signals in three orthogonal directions are given in the diffraction plane, thereby providing an optimized design to achieve EMCD measurements. Finally, we discuss the signal-to-noise-ratio and required electron dose in order to obtain a measurable EMCD signal for 2D vdW magnets. Our results provide a feasibility analysis and guideline to measure 2D vdW magnets in future experiments.

Keywords: Two-dimensional van der Waals magnets, Electron magnetic chiral dichroism, Transmission electron microscopy, signal-to-noise-ratio.

Highlights

- The feasibility analysis of EMCD measurements in three orthogonal directions are conducted for 2D magnets to provide a guide for future experiments under zone axial orientation.
- The low voltage EMCD technique is beneficial to 2D magnets at a ultrathin thickness.
- The number of atomic layers could lead to a strong modulation of EMCD signals under zone axial orientation.
- The slight beam tilt can be utilized to enhance the EMCD signals under zone axial orientation.
- The SNR and required electron dose are quantitatively evaluated for EMCD measurement on 2D magnets.

1. Introduction

The newly-discovered two-dimensional (2D) van der Waals (vdW) crystals with intrinsic magnetism have stimulated intensive studies of magnetic states in 2D limits, triggered by their novel magnetic physics and exciting potential applications in highly efficient nanodevices [1–3]. To date, 2D magnetic crystals are mostly cleavable layered magnetic materials, *e.g.* transition metal halides and transition metal chalcogenides, in which the $3d$ transition metal elements are magnetically coupled with each other both in interlayer and intralayer [4–6]. The long-range magnetic order in 2D vdW crystals, *e.g.* ferromagnetic or antiferromagnetic orders, could sustain at a finite temperature by strong magnetic anisotropy as a result of the balance between spin fluctuations and thermal fluctuations [3]. Moreover, these 2D magnetic crystals have demonstrated diverse magnetic states that depend on the crystal structures and the manifested thickness [6] or stacking [7]. These magnetic orderings could also be modified through external perturbations, *e.g.* strain, chemical doping, magnetic field, electrical gating and proximity effects [3]. Probing these magnetic states is essential to understand the physical origin of magnetism in 2D limits and further build the connections with their atomic configurations, chemistry and electronic structure.

The key challenge of measuring magnetism in 2D crystals arises from the small volume of the sample, typically several atomic layers in thickness and micro-size in lateral dimensions. Thus it is hardly accessible to obtain detectable signals by conventional magnetic characterization techniques, such as the vibrating sample magnetometry (VSM), superconducting quantum interference device (SQUID) magnetometry, magnetic force microscopy (MFM) and neutron scattering. The spatially-resolved magnetic measurements are practically necessary with a resolution varying from microscale to nanoscale. Atomic scale resolution measurements are also needed when it comes to explore the local spin configurations. At present, several powerful techniques have already been widely used to probe the 2D magnetism, including the magneto-optical Kerr microscopy (MOKE) [1,2,8], X-ray magnetic circular dichroism (XMCD) [9], spin-polarized scanning tunneling microscopy (SP-STM) [7], magnetic exchange force microscopy (MExFM) [10], scanning nano-SQUID [11], scanning single-spin microscopy based on diamond nitrogen-vacancy centers [12] and some other indirect electrical methods [13,14]. Each technique has its own merits and shortcomings (see discussions in Section 2). Introducing new advanced magnetic characterization techniques is still indeed needed for a quantitative high-spatial-resolution measurement with high magnetic sensitivity in three orthogonal directions, in order to provide deep insights into 2D magnetism.

Electron magnetic chiral dichroism (EMCD) was developed for magnetic characterization based on the electron energy-loss spectra (EELS) in the transmission electron microscope (TEM) in 2006 [15,16], as the counterpart of XMCD based on the synchrotron X-ray facilities [17]. The conspicuous high spatial resolution [18–22], even down to atomic scale [23–28], and its combination with some other TEM characterization techniques for crystal structure, electronic structure and chemical compositions, making EMCD a very promising candidate for the measurement of 2D magnets. In this work, we first compare EMCD with these above-mentioned techniques in the aspects of spatial resolution, quantification and three-dimensional measurement of magnetic states. The potential issues of measuring 2D magnets by EMCD are then proposed. Later, we conduct the EMCD simulations on several typical 2D magnets and discuss the experimental design for magnetic measurement in three orthogonal

directions. The influence of experimental factors, including the accelerating voltage, the number of atomic layers and beam tilt, are discussed. Finally, we analyze the signal-to-noise-ratio (SNR) of EMCD signals for ultimately thin 2D magnets.

2. Comparison of magnetic characterization techniques for 2D magnets

2.1 Spatial resolution

The lateral spatial resolution is always limited by the probe size. The experimentally achievable resolution could be down to atomic scale both for MExFM [10] and SP-STM [29], though with surface sensitivity. However, the clean sample surface are required. It is always not applicable for 2D magnets as they are often prepared through mechanical exfoliation. In addition, SP-STM is only suitable for conducting samples. The MOKE technique is nowadays the most widely used tool to measure 2D magnets with extremely high magnetic sensitivity at sub-micrometer resolution [4]. With regard to the magneto-optic effects, the XMCD technique can instead provide a spatial resolution not worse than 15 nm, benefiting from the developed aberrated-optics on the advanced synchrotron radiation light source [17,30,31]. Also, XMCD is free from the diamagnetic background, in comparison with the MOKE technique. These above-mentioned non-destructive optical techniques are sensitive to magnetism beneath the sample surface several nanometers but not detrimental to ultrathin 2D magnets. Scanning nano-SQUID [11] and single-spin microscopy based on diamond nitrogen-vacancy [12] can achieve a spatial resolution of several tens of nanometers through detecting the stray magnetic fields emerging from the sample. The spatial resolution of EMCD is determined by the size of electron beam and normally varies from hundreds of nanometers to several nanometers in the parallel-beam TEM mode and from several nanometers to sub-angstrom in the focused-beam scanning TEM (STEM) mode [32]. Moreover, EMCD is sensitive to the bulk as the high-energy electrons can travel through the entire sample, *i.e.*, from the top to the bottom surfaces.

2.2 Quantification of magnetic parameters

The signals detected by these aforementioned techniques can be correlated with magnetic parameters, e.g., magnetization and magnetic moment, based on the phenomenological models and other reasonable assumptions. However, the ambiguously quantitative relationship between the Kerr rotation angle and magnetization are discussed in MOKE measurements for 2D magnets [6]. Similarly, in SP-STM, spin polarized currents cannot be easily correlated with magnetic moments [29]. Scanning nano-SQUID [11] and single-spin microscopy [12] can quantitatively measure the magnetization through in association with the measured local stray fields. The spin and orbital magnetic moments can be calculated from the XMCD [33,34] and EMCD [35,36] signals with element specificity based on the sum rules. Note that the EMCD signal is modulated by the dynamical diffraction effects due to multiple scattering in crystals, complicating quantitative EMCD measurements [37–44], and simulations are always conducted to interpret the experimental results. However, the ratio of the orbital and spin magnetic moment m_L/m_S can be directly extract from the experimental EMCD signals without simulations as it is independent of the dynamical coefficients [35,36].

2.3 Three-dimensional magnetic measurement

The capability of three-dimensional magnetization measurements is highly demanded to explore the intrinsic magnetism and its response to external magnetic field in 2D magnets. Practically, most of the techniques can provide one-, two-, or three-dimensional magnetization, which is always determined by the associated experimental setup and the underlying physical principle. For instance, SP-STM can in principle give the out-of-plane and in-plane magnetic signals [29]; the optical MOKE and XMCD techniques mostly have access to detect the out-of-plane magnetization as a function of external magnetic field perpendicular to the sample surface, though 3D measurements with dedicated experimental designs have already been demonstrated for magnetic nanostructures[45,46]. Scanning nano-SQUID [11] and single-spin microscopy [12] are only sensitive to the out-of-plane magnetization. EMCD has been developed to measure both the out-of-plane and in-plane magnetization simply by shifting the detector positions [47,48]. In the Lorentz mode (magnetic-field-free in the sample position) in TEM, EMCD is able to measure the magnetization evolution under an external magnetic field applied by the partially excited objective lens [48].

2.4 Notes on EMCD for 2D magnets

As discussed above, EMCD is able to provide quantitative magnetic parameters at high spatial resolution in three directions. 2D magnets can serve as an ideal platform to demonstrate these capabilities. It is worth to note that these following issues have to be kept in mind when designing and performing EMCD experiments. First, EMCD is conventionally conducted under the two-beam or three-beam conditions in order to reduce the dynamical diffraction effects [16,37,49,50]. Instead, 2D magnets are always stabilized at around zone axial (ZA) orientation in their as-prepared status, and thus ZA diffraction geometry are more practicable for EMCD experiments, as schematically shown in **Fig. 1**. Experimental conditions, *e.g.* sample orientation, detector positions and collection angle, should be carefully tackled under the ZA condition as discussed before [51]. By subtracting the two EEL spectra from conjugated positions (dotted circles in **Fig. 1)**, the EMCD signal is obtained. Second, although high accelerating voltage generally leads to an enhancement of EMCD signals [52], a low accelerating voltage is necessary to reduce the electron-beam-induced irradiation damage on 2D materials. Besides, the double differential cross-sectional scattering (DDSCS) for inelastic electrons will increase at a low accelerating voltage, giving rise to a higher intensity of EELS signals. Last but the most important issue is whether the atomic-layer-thick 2D magnets could provide measurable EMCD signal upon noise especially at high spatial resolution. Given the pretty low SNR of EMCD signals, it is highly desired to discuss the feasibility in experiments on 2D magnets. Note that EMCD is commonly available to magnetic elements with the characteristic energy-loss less than several thousand eV, covering most of the 2D magnets containing 3d transition metal elements.
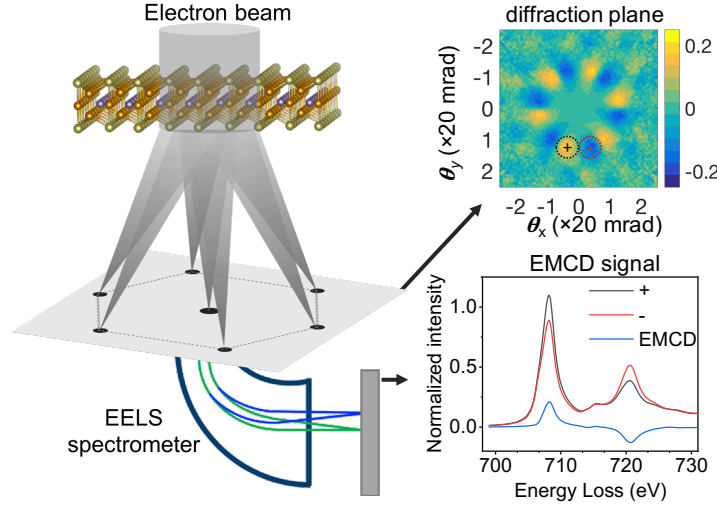
Fig. 1. Schematic illustration of EMCD experiments on 2D magnets under zone axial orientation (left). The dotted circles represent two conjugated detector positions ("+" and "-") in the diffraction plane (upper right). The EMCD signal (lower right) is the difference of EELS signals from "+"and "-" positions.

2.5 Other techniques in the TEM

At the end of this part, we give a brief discussion of the phase contrast based magnetic imaging techniques in the TEM, *e.g.* Lorentz microscopy, off-axis electron holography and differential phase contrast (DPC), for which the phase of the electron beam is altered by the magnetic vector potential of the sample. Taking the example of Fe_3GeTe_2 with the in-plane saturation induction of ~0.4 T [13] and the thickness of 1.63 nm (two atomic layers), the magnetic phase gradient $d\varphi/dx$ is estimated to be $2\pi/6000$ rad nm^{-1}, and the deflection angle of the electron beam is estimated to be 0.77 μrad and 0.30 μrad at 60 kV and 300 kV, respectively. Off-axis electron holography could directly measure the phase shift [53] while the estimated $d\varphi/dx$ is beyond the upper limit of phase sensitivity reported in literatures ($2\pi/1000$) [54]. DPC can map the magnetic contrast through measuring the deflection of central diffraction disk. Though the estimated deflection angles are within the theoretical detection limitation of 0.028 μrad [55,56], there is still no experimental proof of such an extremely high sensitivity. Meanwhile, the estimated deflection angle is almost four orders of magnitude less than a typical Bragg scattering angle. They could hardly be distinguished in the Foucault mode of Lorentz-TEM imaging. While for the Lorentz Fresnel imaging technique, the magnetic contrast is always present at the domain walls. Assuming a domain wall with the width of 10 nm for Fe_3GeTe_2, the defocus values should be as large as ~8 mm and ~20 mm at 60 kV and 300 kV for 10% difference of relative intensity across the domain wall [57], respectively, which might have already been beyond the limit of microscope. Last but not least, all of these techniques are only sensitive to the in-plane magnetization (perpendicular to the electron beam), which would probably become another bugbear for 2D magnets that are always with strong out-of-plane anisotropy.

3. EMCD simulations on 2D magnets

In this section, we have conducted EMCD simulations on several typical 2D magnets under nearly-parallel electron beam illumination conditions, which is able to provide measurements at a spatial resolution in the range from hundreds of nanometers to several nanometers on a modern microscope. The distribution and intensity of EMCD signals in the diffraction plane from three orthogonal directions of the magnetization are discussed with respect to experimental factors under ZA diffraction geometry, *e.g.* accelerating voltage, the number of atomic layers and beam tilt.

3.1 Crystal structure

Fig. 2 shows five atom models of 2D magnets both in the perspective (upper panel) and projective (middle panel, along the *c* axis) view, respectively, for $Cr_2Ge_2Te_6$, CrI_3, $CrBr_3$, Fe_3GeTe_2 and VSe_2 with the origin of magnetism from the $3d$ transition elements. These materials have already been widely studied [1,2,7,8,58]. All of them have a similar layered hexagonal structure with the easy cleavage plane perpendicular to the *c* axis. Atomic-layer-thin samples, even down to one or two layers, can thus be prepared by mechanical exfoliation or molecular beam epitaxy. Different stacking orders through interlayer rotation or translation are believed to be existing in these 2D magnets. Layer dependent magnetic properties, such as the magnetization, magnetic anisotropy, magnetic ordering and ordering temperature, have been reported [6]. Therefore, EMCD simulations should be performed as a function of the number of atomic layers. We take these five different systems as EMCD signals are strongly dependent on the atomic species and their arrangements, in particular when EMCD is performed under the ZA diffraction geometry.
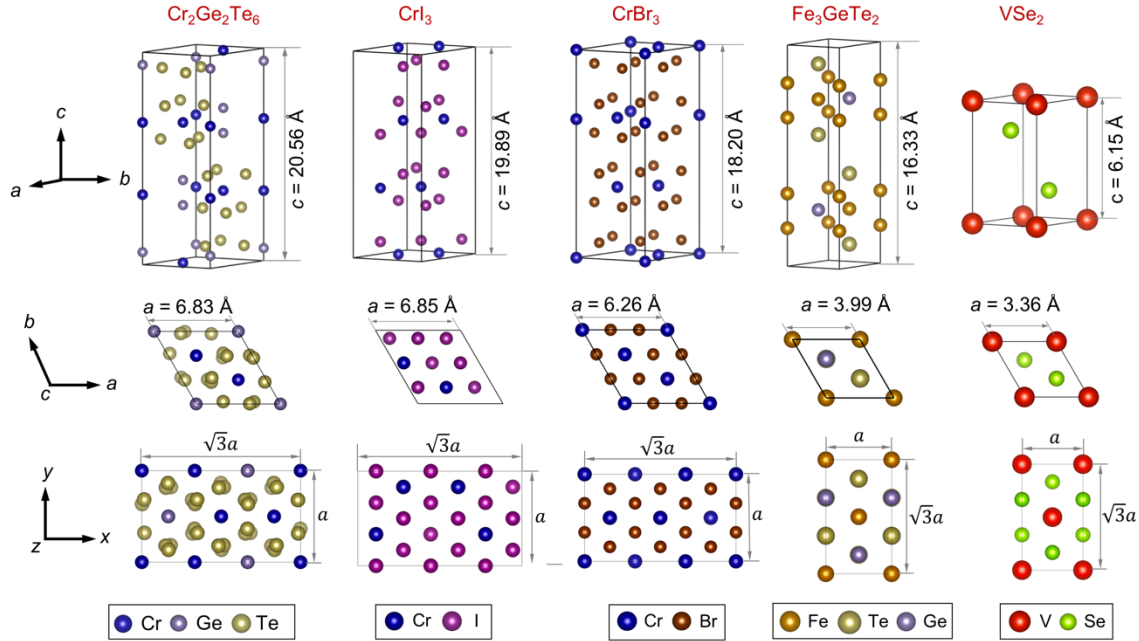

Fig. 2. Atom models of 2D magnets: $Cr_2Ge_2Te_6$, CrI_3, $CrBr_3$, Fe_3GeTe_2 and VSe_2. The upper panel shows the primary unit cells in the perspective view. The number of atomic layers in the primary unit cells is 3, 3, 3, 2 and 1 for $Cr_2Ge_2Te_6$, CrI_3, $CrBr_3$, Fe_3GeTe_2 and VSe_2 along the *c* axis, respectively. The middle panel shows the corresponding projections along the [001] direction (*c* axis). The bottom panel shows the orthogonal supercells cut from the primary unit cells, which are used for EMCD simulations.

3.2 Details of EMCD simulations

EMCD simulations are conducted with the software MATS v2, in which the algorithm has been optimized and the computational speed has been significantly improved [59,60]. In addition, the combination of the multi-slice method for incoming beam and the Bloch-wave method for outgoing beam is introduced [61], which is beneficial for the simulations of ultrathin 2D magnets with a fixed number of atomic layers in thickness. The orthogonal supercells with different numbers of atomic layers are constructed by taking the c axis as the desired ZA orientation. First, the orthogonal supercells with minimal lateral dimension are cut from the primary unit cells (middle panel of **Fig. 2**), with the sizes of $\sqrt{3}a \times a \times c$, $\sqrt{3}a \times a \times c$, $\sqrt{3}a \times a \times c$, $a \times \sqrt{3}a \times c$ and $a \times \sqrt{3}a \times c$ for $Cr_2Ge_2Te_6$, CrI_3, $CrBr_3$, Fe_3GeTe_2 and VSe_2, respectively, as shown in the bottom panel of **Fig. 2**. Then, the shift of 1/6, 1/6, 1/6, 0 and 1/4 of the cell size are applied along the c axis for all of these supercells, respectively, in order to shift the atomic planes to the inner of the supercells for multi-slice calculations. Finally, the supercells with different numbers of atomic layers are directly segmented along the c axis, ranging from 1 to 9 in our simulations. Microscope parameters are set with the convergence angle of 0.5 mrad (nearly-parallel beam illumination), and the accelerating voltage of 60 and 300 kV. The supercells used for simulations are with the sizes of $18\sqrt{3}a \times 32a$ (a = 6.827 Å), $18\sqrt{3}a \times 32a$ (a = 6.847 Å), $18\sqrt{3}a \times 32a$ (a = 6.260 Å), $32a \times 18\sqrt{3}a$ (a = 6.910 Å) and $40a \times 24\sqrt{3}a$ (a = 5.810 Å) for $Cr_2Ge_2Te_6$, CrI_3, $CrBr_3$, Fe_3GeTe_2 and VSe_2, respectively. The electron energy-loss at EELS L_3 edge is taken for each 3d transition element, $i.e.$ 575 eV for Cr, 708 eV for Fe and 513 eV for V. The simulated ranges in the diffraction plane are 50 mrad $\times$ 50 mrad at 60 kV and 20 mrad $\times$ 20 mrad at 300 kV, respectively. The slight tilt of the sample is achieved by tilting the electron beam in simulations. The relative intensity of EMCD signal is defined as the ratio between EMCD signals and nonmagnetic signals. The x, y and z directions are defined in the bottom panel of **Fig. 2**. The Mx, My and Mz EMCD signals are simulated simultaneously assuming that they have the same magnitude of magnetization (unit one).

3.3 Accelerating voltage

Fig. 3 shows the simulated relative intensity of EMCD signals from three directions at 60 kV and 300 kV in the diffraction plane, respectively. Here we take the [001] ZA orientation and the sample thickness of two atomic layers for all of these material systems. The similarity in distributions of EMCD signals in the diffraction plane are due to the similar symmetry of their crystal structures. On the other hand, we can see different symmetries of the distributions of the relative intensity of EMCD signals from three directions, $i.e.$ $\sigma_{Mag,x}/\sigma_{Nonmag}$, $\sigma_{Mag,y}/\sigma_{Nonmag}$ and $\sigma_{Mag,z}/\sigma_{Nonmag}$, where σ_{Mag} and σ_{Nonmag} are the scattering cross-sections of magnetic and nonmagnetic components, respectively. The $\sigma_{Mag,x}/\sigma_{Nonmag}$ ($\sigma_{Mag,y}/\sigma_{Nonmag}$) EMCD signal is antisymmetric with respect to the x (y) axis, respectively. It is determined by the terms of momentum transfer ($\mathbf{q} \times \mathbf{q}'$) in the formula of DDSCS that the $\sigma_{Mag,x}/\sigma_{Nonmag}$ ($\sigma_{Mag,y}/\sigma_{Nonmag}$) EMCD signal is contributed by q_y (q_x) and q_z [47,48]. More importantly, the sign of the $\sigma_{Mag,x}/\sigma_{Nonmag}$ ($\sigma_{Mag,y}/\sigma_{Nonmag}$) EMCD signals remains unchanged in the upper (left) and lower (right) half of the diffraction plane, which is very beneficial for signal acquisition in experiments. A large aperture can be used in order to get signals with high intensity and

SNR, as schematically indicated with dotted circles in **Fig. 3**. However, in the case of $\sigma_{Mag,z}/\sigma_{Nonmag}$ EMCD signal, the symmetry of the distribution is not only determined by the momentum transfer of q_x and q_y but also the symmetry of atomic arrangement of magnetic elements in the crystal. Three antisymmetric mirrors are indicated with black lines in **Fig. 3**. The complex distributions with the crossfade sign of $\sigma_{Mag,z}/\sigma_{Nonmag}$ EMCD signals can be observed in each quadrant of the diffraction plane. The collection angle is therefore limited and the positions of EELS entrance aperture should be accurately set in experiments, as indicated with dotted circles in **Fig. 3**; otherwise the EMCD signals with opposite signs will cancel out and lead to the reduction of signal intensity and SNR. In addition, the $\sigma_{Mag,z}/\sigma_{Nonmag}$ EMCD signals are weaker than that of $\sigma_{Mag,x}/\sigma_{Nonmag}$ and $\sigma_{Mag,y}/\sigma_{Nonmag}$ EMCD signals according to the color bar in **Fig. 3**. Therefore, a relatively longer exposure time is needed for the $\sigma_{Mag,z}/\sigma_{Nonmag}$ EMCD signal acquisition in experiments.

Furthermore, the effect of the accelerating voltage can be observed. The enhancement of EMCD signals by a high accelerating voltage [52] is no longer applicable for 2D magnets with a ultrathin thickness. On the contrary, at a low accelerating voltage, we obtain the distributions with higher intensity of EMCD signals in the diffraction plane, in particular for $\sigma_{Mag,x}/\sigma_{Nonmag}$ and $\sigma_{Mag,y}/\sigma_{Nonmag}$ EMCD signals in **Fig. 3**. This could be attributed to the increased DDSCS, as well as its slow attenuation as a function of the scattering angle. Therefore, a low accelerating voltage is an optimal choice for EMCD measurements on 2D magnets.

Note that the simulated EMCD signals from all of the three magnetization directions are overlapped with each other in the diffraction plane. The experimental EMCD signals are a product of the simulated EMCD signals and the sample magnetization (**M**). Therefore, there is no need to make the separation if the magnetization is only along one of the three directions, *e.g.* $Mx = My = 0, Mz \neq 0$, which is always the case in the TEM mode with the objective lens on. Otherwise, it is necessary to separate the EMCD signals in three directions.

To attain this goal, the symmetry of the signal distributions are always used to cancel out the unwanted signals through selecting the detector positions. Here we propose a set of detector setups to separate them as shown in **Fig. 4**, taking the example of the VSe₂. For pure EMCD signals from x direction, we put the conjugate detectors on the y axis in **Fig. 4**(a), as the $\sigma_{Mag,z}/\sigma_{Nonmag}$ and $\sigma_{Mag,y}/\sigma_{Nonmag}$ are antisymmetric with respect to the y axis. For pure EMCD signals from y direction, four detectors (the red and black groups) are set on the three-fold symmetry axis in **Fig. 4**(b). They are also symmetric with respect to the x and y axis, respectively. Consequently, the summation of the signals from two red (black) circles will only contain the EMCD signals from y direction. It is the similar case for pure EMCD signals from z direction, and four detectors are set with respect to the y axis as shown in **Fig. 4**(c). Although the detector setup is designed for the hexagonal crystal here, the solution will also be accessible to other crystals with different symmetries, *e.g.* the cubic crystal with a four-fold symmetry.
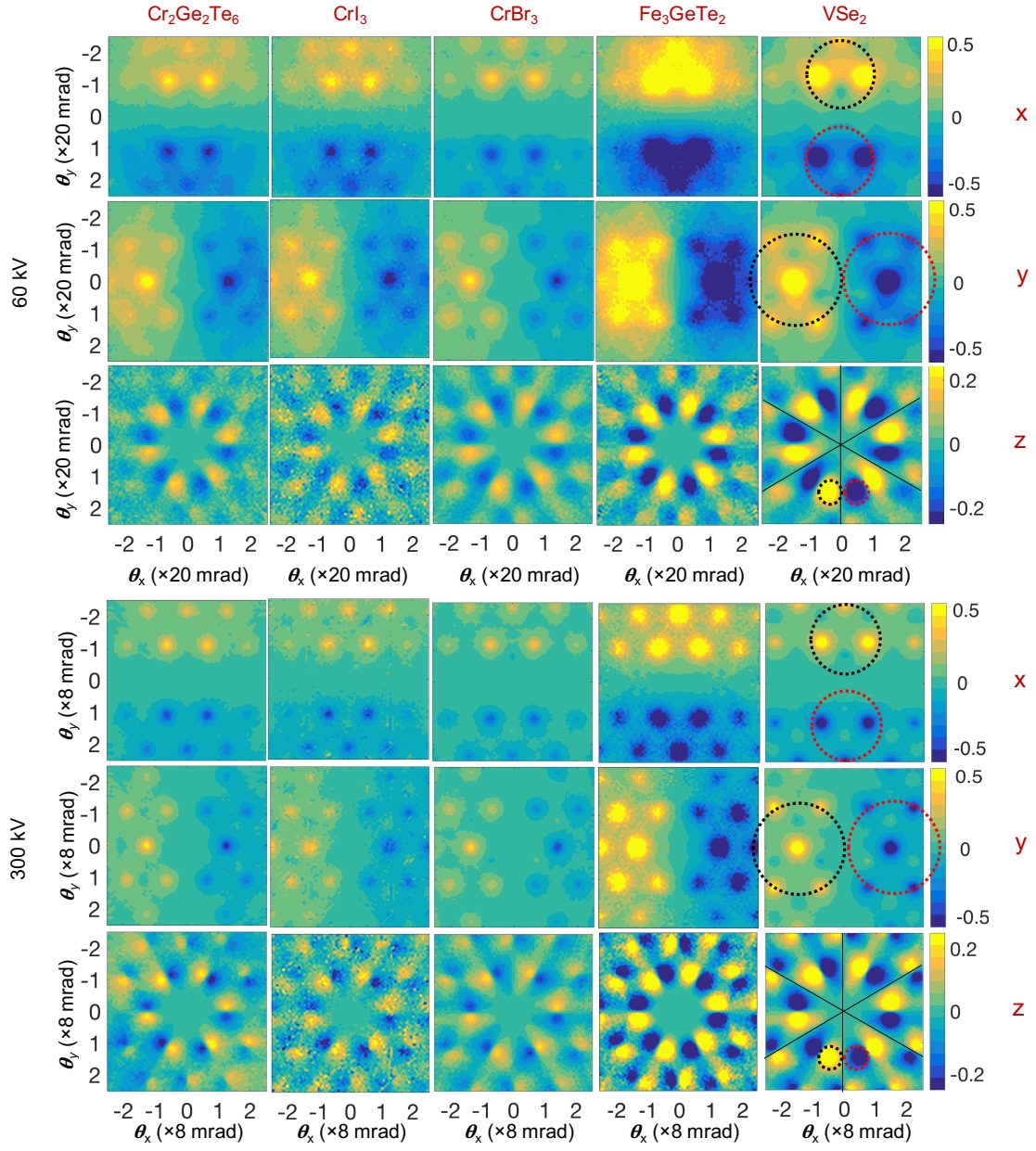
Fig. 3. The simulated distributions of the relative intensity of EMCD signals in the diffraction plane at 60 kV (upper panel) and 300 kV (lower panel) under [001] zone axial orientation. The samples are all two-atomic-layer thick. The EMCD signals are displayed in x, y and z directions (labeled on the right of the each panel). Black dotted circles represent the conjugated detector positions. Black solid lines indicate the symmetric mirrors of EMCD signals from z direction. The ranges in the diffraction plane are 50 mrad $\times$ 50 mrad and 20 mrad $\times$ 20 mrad at 60 kV and 300 kV, respectively.
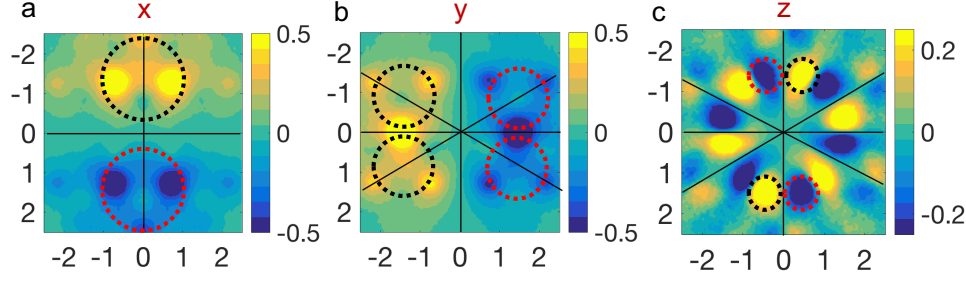
Fig. 4. The detector setup for the separation of EMCD signals from all of the three directions, taking the example of VSe_2 with the thickness of two atomic layers. The black and red dotted circles represent the conjugate detector positions. The black solid lines indicate the symmetric mirrors of EMCD signals in the diffraction plane. The ranges in the diffraction plane are 50 mrad $\times$ 50 mrad at 60 kV, respectively.

3.4 Sample thickness

Thickness and stacking order dependent magnetic properties have already been observed in 2D magnets [6]. It is determined by the number of atomic layers and the intralayer coupling. The atomic arrangement and sample thickness can be directly measured by imaging or diffraction techniques in the TEM. Here, we discuss the EMCD signals under different numbers of atomic layers at 60 kV in **Fig. 5**. It can be seen that the distribution of EMCD signals show small variations with the increasing number of atomic layers from 1 to 9, in contrast to the case for a thicker sample [51] where the sign of EMCD signals are often reversed with the increasing thickness under ZA orientation.

The intensity of EMCD signals are always modulated by the sample thickness. The integrated signals within the virtual aperture (as schematically indicated in **Fig. 3**) are shown in **Fig. 6**, with the collection semi-angle of approximately 18 mrad, 23 mrad and 5 mrad for *x*, *y* and *z* directions, respectively. The smaller collection semi-angle for $\sigma_{Mag,z}/\sigma_{Nonmag}$ EMCD signals is limited by its complex distribution in the diffraction plane, which consequently affects the SNR (see discussions in section 4). The $\sigma_{Mag,x}/\sigma_{Nonmag}$ and $\sigma_{Mag,y}/\sigma_{Nonmag}$ EMCD signals are higher than that of the $\sigma_{Mag,z}/\sigma_{Nonmag}$ EMCD signal, which is beneficial for experimental measurements of in-plane 2D magnetic states in the magnetic-field-free environment [48,62]. The relative intensity of EMCD signals exhibit Pendellösung oscillations that are caused by the channeling and dechanneling effects of dynamical diffraction effects with respect to the sample thicknesses in **Fig. 6**. The $\sigma_{Mag,x}/\sigma_{Nonmag}$, $\sigma_{Mag,y}/\sigma_{Nonmag}$ and $\sigma_{Mag,z}/\sigma_{Nonmag}$ EMCD signals show a similar variation trend as they follow the same diffraction conditions. The intensity of EMCD signals first increase, then tend to be flat, and later decrease with respect to the increasing thickness, indicating the strong modulations even in a small window of thickness under the ZA orientation. In addition, the difference among several crystal structures can be observed, attributing to different atomic species and arrangements of magnetic elements. For instance, the different stacking ordering of CrI_3 and $CrBr_3$ [7] along the thickness direction leads to different channeling effects and the resultant intensity of EMCD signals. The intensity of EMCD signals for Fe_3GeTe_2 decreases at a smaller sample thickness. This is due to a smaller extinction distance arising from the heavy elements along the atomic column. The reversed sign of EMCD signals is also observed around the transmitted beam at a larger thickness for Fe_3GeTe_2 in **Fig. 5**. These results

definitely demonstrate the strong dependence of EMCD signals on crystal structures, emphasizing the necessity of prior simulations to interpret experimental data properly [40,63] for ZA EMCD measurement even with a ultrathin sample thickness.
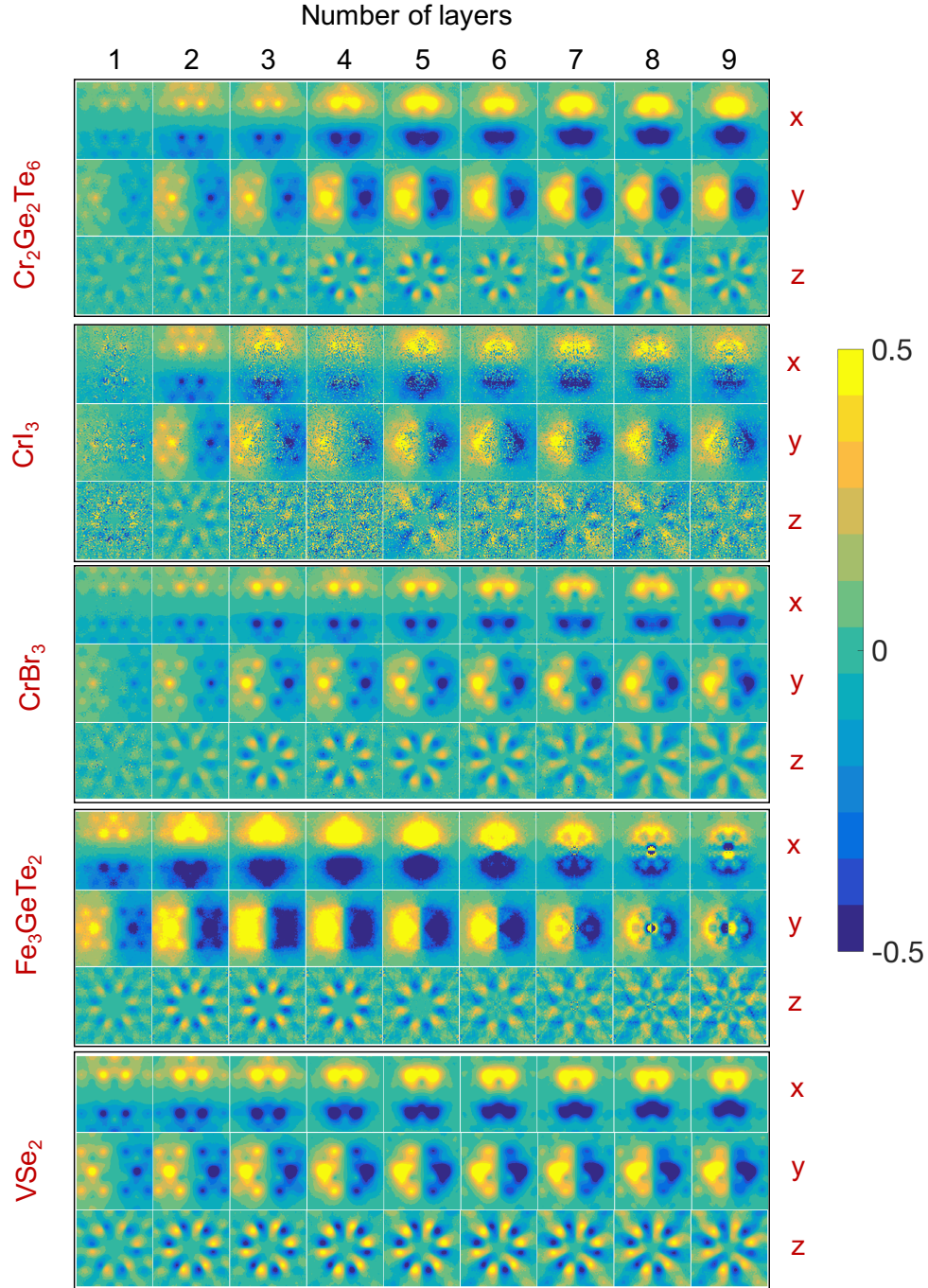

Fig. 5. Simulated distributions of the relative intensity of EMCD signals in the diffraction plane with respect to the number of atomic layers from 1 to 9. The accelerating voltage is 60 kV. EMCD signals in *x*, *y* and *z* directions are displayed (labeled on the right of the each panel). All of the ranges in the diffraction plane are 50 mrad × 50 mrad.

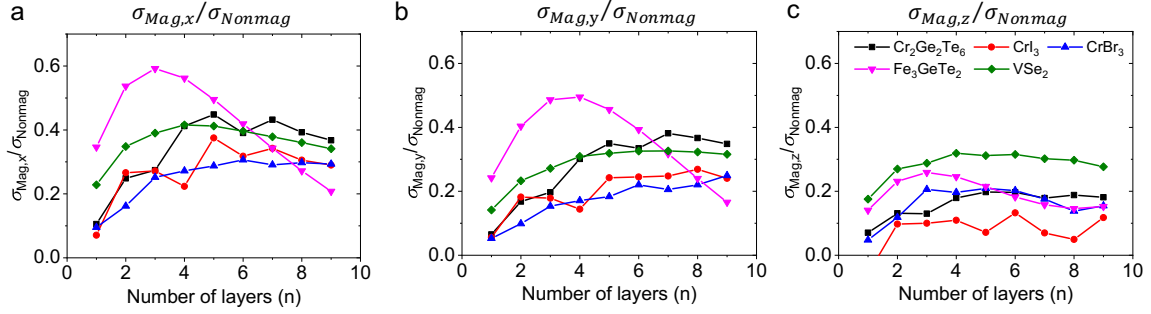**Fig. 6.** Simulated relative intensity of EMCD signals in *x*, *y* and *z* directions at 60 kV as a function of the number of atomic layers by integrating the signals in **Fig. 5** according to the positions of virtual apertures (marked with circles in **Fig. 3)**, respectively. The collection semi-angles are approximately 18, 23 and 5 mrad for *x*, *y* and *z* EMCD signals, respectively.

3.5 Beam tilt

Under the ZA orientation, EMCD signals are quite sensitive to the dynamical diffraction effects. It is always worth to optimize experimental conditions in order to improve the intensity and SNR of EMCD signals, such as the sample thickness, sample orientation, incident direction of electron beam and detector positions. Here we attempt to make use of the beam tilt to enhance the EMCD signals. The beam tilt can be easily introduced by slightly tilting the sample along a specific direction from the ZA orientation in experiments. It has been ever reported that the beam tilt can reduce the channeling effects and consequently enhance the ECMD signals at atomic resolution, regardless of its counter effects on the increased degree of delocalization [64]. Since we take the nearly-parallel electron beam here, the delocalization is not pronounced. The simulated EMCD signals from $CrBr_3$ as a function of the sample thickness and tilting angle are shown in **Fig. 7**. The beam is tilted along the *y* axis, and the up-down symmetry of $\sigma_{Mag,x}/\sigma_{Nonmag}$ EMCD signals is thus broken. Here we only discuss the $\sigma_{Mag,y}/\sigma_{Nonmag}$ and $\sigma_{Mag,z}/\sigma_{Nonmag}$ EMCD signals. Similar effects on $\sigma_{Mag,x}/\sigma_{Nonmag}$ EMCD signals can be achieved just by changing the tilting axis to *x* axis.

In the lower panel of **Fig. 7**, the $\sigma_{Mag,y}/\sigma_{Nonmag}$ EMCD signals are reduced at the upper half of the diffraction plane (opposite to the tilting direction), but a bit enhanced at the lower half of the diffraction plane (in the tilting direction). By averaging the signals in the virtual apertures (indicated in **Fig. 3**), the enhancement of $\sigma_{Mag,x}/\sigma_{Nonmag}$ EMCD signals can be negligible in **Fig. 8**(a). On the other hand, for $\sigma_{Mag,z}/\sigma_{Nonmag}$ EMCD signals, the enhancement is remarkable as guided by the virtual apertures in the upper panel of **Fig. 7**. The averaged values in the virtual apertures are shown in **Fig. 8**(b). The enhancement ratio can be as high as two- or three-times at a large sample thickness, though not obvious when the sample is one or two atomic-layer thin. This could be due to the fact that the slight change of incident condition subtly alters the channeling effects. In addition, the distributions of $\sigma_{Mag,z}/\sigma_{Nonmag}$ EMCD signals are substantially modified in the diffraction plane, in particular at a large sample thickness, where the sign of $\sigma_{Mag,z}/\sigma_{Nonmag}$ EMCD signals are reversed in many regions in **Fig. 7**. When the sample is 9-atomic-layer thin, the left and right half of the diffraction plane

have a large area with the high intensity of $\sigma_{Mag,z}/\sigma_{Nonmag}$ EMCD signals. It is anticipated that beam tilt can effectively help increase the SNR of experimental EMCD signals.
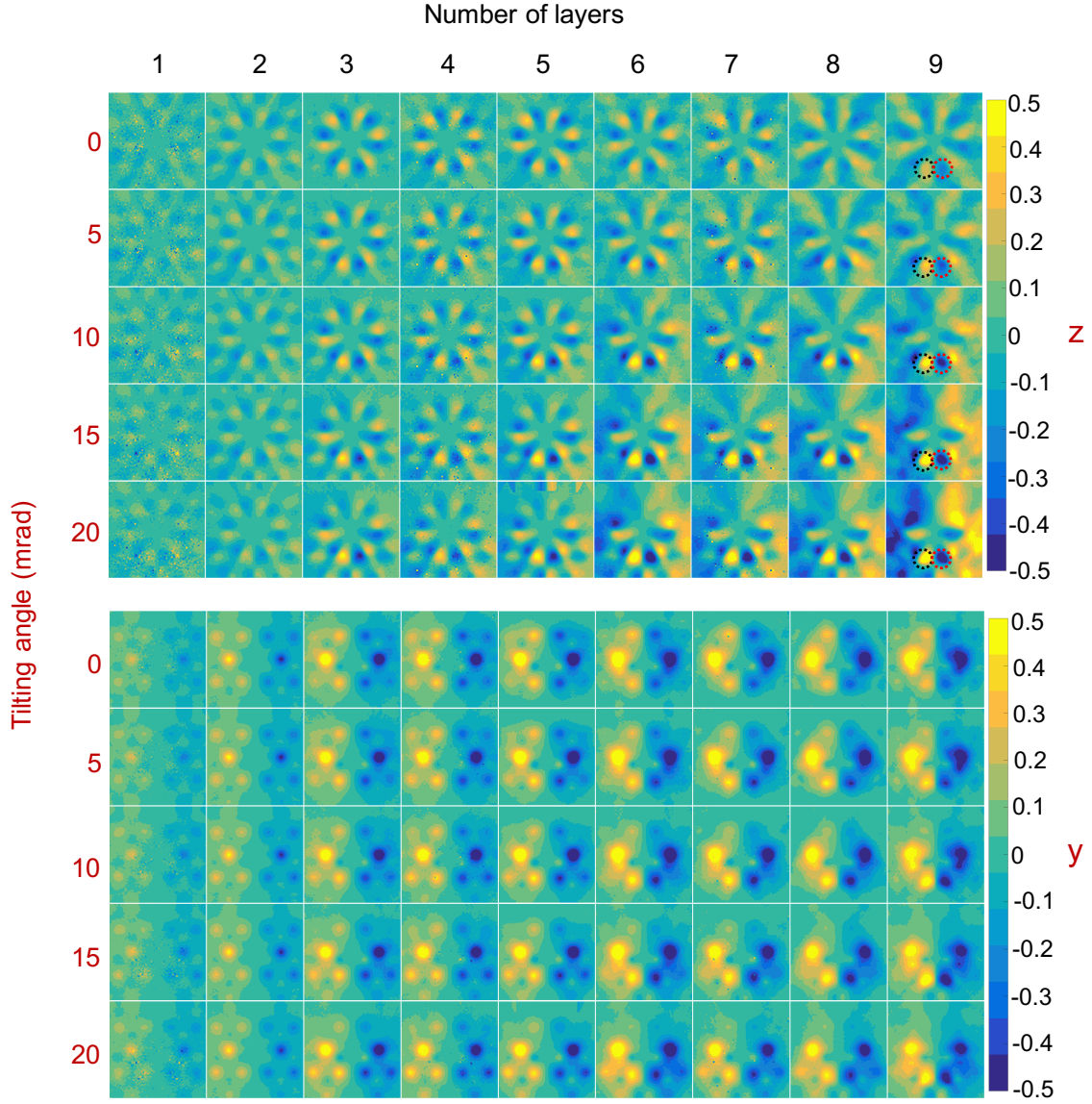

Fig. 7. Simulated distributions of the relative intensity of EMCD signals for y and z directions in the diffraction plane as a function of tilting angle and the number of atomic layers at 60 kV for $CrBr_3$. The tilting direction is along the -y axis. The tilting angle varies between 0, 5, 10, 15 and 20 mrad, as labeled on the left side of the panel. The ranges in the diffraction plane are 50 mrad $\times$ 50 mrad.
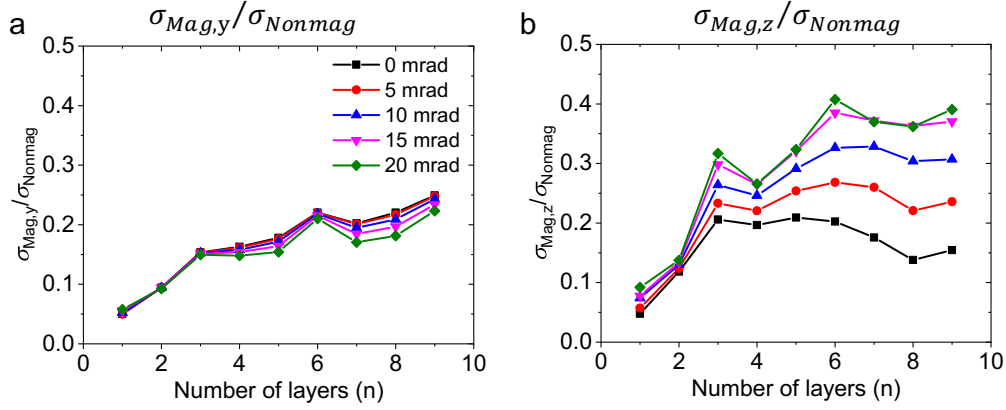
Fig. 8. Simulated relative intensity of EMCD signals in y and z directions for CrBr$_3$ at 60 kV as a function of the number of atomic layers and tilting angle (along the - y direction) by averaging the signals in **Fig. 7** according to the positions of virtual apertures (marked with circles in **Fig. 3)**, respectively. The collection semi-angles are approximately 23 and 5 mrad for EMCD signals in y and z directions, respectively.

4. SNR of EMCD signals for 2D magnets

The notoriously low signal intensity and SNR are the most striking issues for EMCD measurements. It becomes extremely challenging when the sample is atom-layer thin. On the other hand, low dose EMCD are indeed required as the weak intralayer bonding can be easily broken by electron-beam-induced irradiation damage. Therefore, the SNR and dose-dependent EMCD signals should be discussed to provide a feasibility analysis of measuring 2D magnets experimentally. The SNR for EMCD signals is defined as follows [26,65–67]:

$$SNR = \frac{2I_{Mag}}{\sqrt{2I_{Nonmag}}} = \frac{2\frac{M}{N}\frac{\sigma_{Mag}}{\sigma_{Nonmag}}C_{L_3}}{\sqrt{2(C_{L_3} + C_{bkg})}}$$

where I_{Mag} and I_{Nonmag} represent the intensity of magnetic EMCD and nonmagnetic EELS signals, respectively. The factor of two is produced by the subtraction or addition of EELS signals from two conjugate positions in order to obtain pure EMCD signals or nonmagnetic EELS signals, respectively. M/N is the ratio between the magnetic and nonmagnetic components, which is determined by the intrinsic electronic properties of 3d magnetic elements, $e.g.$, magnetic moments, number of holes and spin-orbital coupling, as described elsewhere [65]. Here 0.15 is taken for M/N. σ_{Mag} and σ_{Nonmag} are the simulated intensity of EMCD signals as discussed above, which is dependent on the crystal structure, thickness, diffraction conditions, detector position θ_{xy} and collection angle β. C_{L_3} and C_{bkg} are the intensity of L_3 peak and background of EELS, respectively. Here we neglect the C_{bkg} for simplification, which is always a few times smaller than C_{L_3} for ultrathin sample. SNR can then be simplified as follows,

$$SNR = \frac{M}{N}\frac{\sigma_{Mag}}{\sigma_{Nonmag}}\sqrt{2C_{L_3}}$$

For two-atomic-layer-thin CrBr$_3$, taking the assumption of SNR > 3 for a visible signal, C_{L_3} is

estimated to be larger than 12500 for EMCD signal in z direction, 9000 and 20000 for EMCD signals in x and y directions, respectively, according to M/N = 0.15 and the relative intensity of EMCD signals $(\sigma_{Mag}/\sigma_{Nonmag})$ in **Fig. 6**. The EMCD signal can be measured when the electron counts at L_3 edge exceed these values. It can be achieved by increasing either the beam current or the exposure time. Furthermore, electron counts can be correlated with the dose of electron beam, and C_{L_3} can then be expressed below:

$$C_{L_3} = \frac{I_{beam}\Delta t}{e} f(\Delta E, \theta_{xy}, \beta, T)$$

Where I_{beam} is the electron beam current and Δt is the exposure time, e is the elementary charge, T is the sample thickness. Note that electron counts for EELS is not equivalent to the dose of the incident electron beam. The intensity of the EELS signal is exponentially decayed with the increasing energy loss and a majority of incident electrons undergo elastic scattering. Therefore, only a fraction of electron dose ($\sim 1 \times 10^{-4}$) empirically contributes to the L_3 at the energy loss of 500 – 800 eV when the sample thickness is 50 nm for $3d$ transition metals [68]. In addition, the EMCD signals are always collected using an off-axis aperture as marked with circles in **Fig. 3**, thus leading to a further reduction. Here, we use the factor $f(\Delta E, \theta_{xy}, \beta, T)$ to describe the transfer efficiency between the incident electron beam dose and recorded electron counts of EELS. It is a function of the energy loss, detector position, collection angle and sample thickness. Assuming that C_{L_3} is linearly increased with T for ultrathin sample, $f(\Delta E, \theta_{xy}, \beta, T)$ can be expressed as follows:

$$f(\Delta E, \theta_{xy}, \beta, T) = \frac{N(\Delta E, \theta_{xy}, \beta)}{N(\Delta E)} \frac{T}{50} \times 1 \times 10^{-4}$$

where $N(\Delta E, \theta_{xy}, \beta)$ is the accumulating intensity of nonmagnetic signals within the virtual aperture positioned at θ_{xy} with the collection angle of β, and $N(\Delta E)$ is the total intensity of nonmagnetic signals in the whole diffraction plane. Following the results in **Fig. 6**, the lower limit of the electron dose $I_{beam}\Delta t$ (SNR > 3) is plotted as a function of the sample thickness for CrBr$_3$ in **Fig. 9**(a). The beam current up to 10^5 pA is needed for EMCD signal in z direction on a single-atomic-layer thin CrBr$_3$ with an exposure time of 10 s, whereas 10^4 pA for EMCD signals in x and y direction. The threshold of the electron dose is decreased by two orders of magnitude when the sample thickness is above three atomic layers, that is a beam current of 10^3 pA for EMCD signal in z direction and 10^2 pA for EMCD signals in x and y directions with an exposure time of 10 s, respectively. This order of the magnitude of the beam current is available even in the STEM mode. The large difference (almost one or two orders) is mainly caused by the terms of $N(\Delta E, \theta_{xy}, \beta)/N(\Delta E)$, which is much smaller for EMCD signals in z direction using a small collection angle as mentioned above. The tilting effects on the electron dose for EMCD in z direction are also shown in **Fig. 9**(b) for CrBr$_3$. As the slight sample tilt enhances the terms of $\sigma_{Mag}/\sigma_{Nonmag}$, the beam current can be reduced even by one order of magnitude for 9-atomic-layer-thick sample.
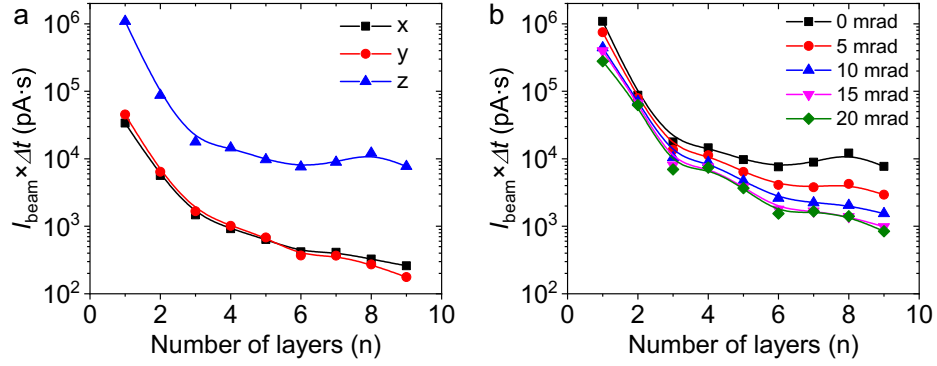
Fig. 9. Estimated beam current with the assumption of SNR > 3 as a function of the number of atomic layers for CrBr$_3$. (a) Under zone axial orientation for EMCD signals in x, y and z directions. (b) With different tilting angles for EMCD signals in z direction.

The electron dose per Å^2 is determined by the probe size, which should be lower than the threshold of irradiation damage for 2D magnets. Assuming an electron dose of 10^4 pA·s with the nearly-parallel illumination condition, the probe with the diameter of 50 nm and 1 nm corresponds to the total electron dose of 3.2×10^5 e/Å^2 and 8×10^8 e/Å^2, respectively. These values are around the threshold of irradiation damage for MoS$_2$ [69], though there is still no relevant research on 2D magnets. Note that direct electron detectors with extremely high detection efficiency installed on the EELS system [68,70,71] will definitely benefit future EMCD measurements on 2D magnets.

Note that SNR > 3 is a very simple assumption here that is only sufficient for the detection of EMCD signal. To quantitatively extract the magnetic moments, a large SNR would be needed. However, the improvement of SNR indicates the significant increase of the electron dose and exposure time. Therefore, the statistical methods are preferred for quantitative measurements if a large amount of signals can be obtained in the experiments. For instance, the least square fitting method [40], the parameter-free multivariate curve resolution (MCR) [39], and the independent component analysis (ICA) [72] have already been demonstrated to obtain high SNR EMCD signals for quantitative measurements.

5. Summary

In summary, we have investigated the magnetic measurements of 2D magnets by EMCD technique in the TEM. Comparisons between the EMCD technique and other magnetic characterization techniques manifest the potential use of the EMCD technique on 2D magnets, with the aim to measure magnetic parameters in three directions at high spatial resolution, in association with complementary measurements on the local atomic structure, electronic structure and chemistry in modern advanced TEMs. EMCD simulations have been conducted to measure 2D magnets in three directions under the zone axial orientation. It has been demonstrated that a relatively low accelerating voltage is not only able to avoid irradiation damages but also provide comparable or even better EMCD signals of 2D magnets at a ultrathin sample thickness. The intensity and distribution of EMCD signals in the diffraction plane are discussed for 2D magnets as a function of the number of atomic layers, indicating strong modulations due to dynamical diffraction effects. In addition, it is also found that a slight beam

(sample) tilt can remarkably enhance the intensity of EMCD signals as a result of the subtle modification of the channeling effects under the zone axial orientation. Furthermore, the SNR and required electron dose are discussed. The typical threshold values, *e.g.* beam current and exposure time, are estimated in order to obtain measurable EMCD signals of 2D magnets in experiments. Our theoretical study provides a feasibility analysis to measure 2D magnets by EMCD technique and is beneficial for future experimental designs and data interpretations.

Reference

[1]   B. Huang, G. Clark, E. Navarro-Moratalla, D.R. Klein, R. Cheng, K.L. Seyler, D. Zhong, E. Schmidgall, M.A. McGuire, D.H. Cobden, W. Yao, D. Xiao, P. Jarillo-Herrero, X. Xu, Layer-dependent ferromagnetism in a van der Waals crystal down to the monolayer limit, Nature. 546 (2017) 270–273. https://doi.org/10.1038/nature22391.

[2]   C. Gong, L. Li, Z. Li, H. Ji, A. Stern, Y. Xia, T. Cao, W. Bao, C. Wang, Y. Wang, Z.Q. Qiu, R.J. Cava, S.G. Louie, J. Xia, X. Zhang, Discovery of intrinsic ferromagnetism in two-dimensional van der Waals crystals, Nature. 546 (2017) 265–269. https://doi.org/10.1038/nature22060.

[3]   K.S. Burch, D. Mandrus, J.-G. Park, Magnetism in two-dimensional van der Waals materials, Nature. 563 (2018) 47–52. https://doi.org/10.1038/s41586-018-0631-z.

[4]   K.F. Mak, J. Shan, D.C. Ralph, Probing and controlling magnetic states in 2D layered magnetic materials, Nature Reviews Physics. 1 (2019) 646–661. https://doi.org/10.1038/s42254-019-0110-y.

[5]   C. Gong, X. Zhang, Two-dimensional magnetic crystals and emergent heterostructure devices, Science. 363 (2019). https://doi.org/10.1126/science.aav4450.

[6]   M. Gibertini, M. Koperski, A.F. Morpurgo, K.S. Novoselov, Magnetic 2D materials and heterostructures, Nature Nanotechnology. 14 (2019) 408–419. https://doi.org/10.1038/s41565-019-0438-6.

[7]   W. Chen, Z. Sun, Z. Wang, L. Gu, X. Xu, S. Wu, C. Gao, Direct observation of van der Waals stacking–dependent interlayer magnetism, Science. 366 (2019) 983–987. https://doi.org/10.1126/science.aav1937.

[8]   Z. Fei, B. Huang, P. Malinowski, W. Wang, T. Song, J. Sanchez, W. Yao, D. Xiao, X. Zhu, A.F. May, W. Wu, D.H. Cobden, J.-H. Chu, X. Xu, Two-dimensional itinerant ferromagnetism in atomically thin Fe 3 GeTe 2, Nature Materials. 17 (2018) 778–782. https://doi.org/10.1038/s41563-018-0149-7.

[9]   W. Yu, J. Li, T.S. Herng, Z. Wang, X. Zhao, X. Chi, W. Fu, I. Abdelwahab, J. Zhou, J. Dan, Z. Chen, Z. Chen, Z. Li, J. Lu, S.J. Pennycook, Y.P. Feng, J. Ding, K.P. Loh, Chemically Exfoliated VSe2 Monolayers with Room-Temperature Ferromagnetism, Advanced Materials. 31 (2019) 1903779.

https://doi.org/10.1002/adma.201903779.

[10] U. Kaiser, A. Schwarz, R. Wiesendanger, Magnetic exchange force microscopy with atomic resolution, Nature. 446 (2007) 522–525. https://doi.org/10.1038/nature05617.

[11] X.R. Wang, C.J. Li, W.M. Lü, T.R. Paudel, D.P. Leusink, M. Hoek, N. Poccia, A. Vailionis, T. Venkatesan, J.M.D. Coey, E.Y. Tsymbal, Ariando, H. Hilgenkamp, Imaging and control of ferromagnetism in LaMnO3/SrTiO3 heterostructures, Science. 349 (2015) 716–719. https://doi.org/10.1126/science.aaa5198.

[12] L. Thiel, Z. Wang, M.A. Tschudin, D. Rohner, I. Gutiérrez-Lezama, N. Ubrig, M. Gibertini, E. Giannini, A.F. Morpurgo, P. Maletinsky, Probing magnetism in 2D materials at the nanoscale with single-spin microscopy, Science. 364 (2019) 973–976. https://doi.org/10.1126/science.aav6926.

[13] Y. Deng, Y. Yu, Y. Song, J. Zhang, N.Z. Wang, Z. Sun, Y. Yi, Y.Z. Wu, S. Wu, J. Zhu, J. Wang, X.H. Chen, Y. Zhang, Gate-tunable room-temperature ferromagnetism in two-dimensional Fe3GeTe2, Nature. 563 (2018) 94–99. https://doi.org/10.1038/s41586-018-0626-9.

[14] S. Jiang, J. Shan, K.F. Mak, Electric-field switching of two-dimensional van der Waals magnets, Nature Materials. 17 (2018) 406–410. https://doi.org/10.1038/s41563-018-0040-6.

[15] C. Hébert, P. Schattschneider, A proposal for dichroic experiments in the electron microscope, Ultramicroscopy. 96 (2003) 463–468. https://doi.org/10.1016/S0304-3991(03)00108-6.

[16] P. Schattschneider, S. Rubino, C. Hébert, J. Rusz, J. Kuneš, P. Novák, E. Carlino, M. Fabrizioli, G. Panaccione, G. Rossi, Detection of magnetic circular dichroism using a transmission electron microscope, Nature. 441 (2006) 486–488. https://doi.org/10.1038/nature04778.

[17] G. van der Laan, A.I. Figueroa, X-ray magnetic circular dichroism—A versatile tool to study magnetism, Coordination Chemistry Reviews. 277–278 (2014) 95–129. https://doi.org/10.1016/j.ccr.2014.03.018.

[18] P. Schattschneider, M. Stöger-Pollach, S. Rubino, M. Sperl, C. Hurm, J. Zweck, J. Rusz, Detection of magnetic circular dichroism on the two-nanometer scale, Physical Review B. 78 (2008). https://doi.org/10.1103/PhysRevB.78.104413.

[19] T. Thersleff, J. Rusz, B. Hjörvarsson, K. Leifer, Detection of magnetic circular dichroism with subnanometer convergent electron beams, Physical Review B. 94 (2016). https://doi.org/10.1103/PhysRevB.94.134430.

[20] D. Song, L. Ma, S. Zhou, J. Zhu, Oxygen deficiency induced deterioration in microstructure and magnetic properties at $Y_3Fe_5O_{12}$/Pt interface, Applied Physics Letters. 107 (2015) 042401. https://doi.org/10.1063/1.4927551.

[21] S. Schneider, D. Pohl, S. Löffler, J. Rusz, D. Kasinathan, P. Schattschneider, L. Schultz, B. Rellinghaus, Magnetic properties of single nanomagnets: Electron energy-loss magnetic chiral dichroism on FePt nanoparticles, Ultramicroscopy. 171 (2016) 186–194. https://doi.org/10.1016/j.ultramic.2016.09.009.

[22] T. Thersleff, S. Muto, M. Werwiński, J. Spiegelberg, Y. Kvashnin, B. Hjörvarsson, O. Eriksson, J. Rusz, K. Leifer, Towards sub-nanometer real-space observation of spin and orbital magnetism at the Fe/MgO interface, Scientific Reports. 7 (2017) 44802. https://doi.org/10.1038/srep44802.

[23] J. Rusz, S. Muto, J. Spiegelberg, R. Adam, K. Tatsumi, D.E. Bürgler, P.M. Oppeneer, C.M. Schneider, Magnetic measurements with atomic-plane resolution, Nature Communications. 7 (2016)

12672. https://doi.org/10.1038/ncomms12672.

[24] Z. Wang, A.H. Tavabi, L. Jin, J. Rusz, D. Tyutyunnikov, H. Jiang, Y. Moritomo, J. Mayer, R.E. Dunin-Borkowski, R. Yu, J. Zhu, X. Zhong, Atomic scale imaging of magnetic circular dichroism by achromatic electron microscopy, Nature Materials. 17 (2018) 221–225. https://doi.org/10.1038/s41563-017-0010-4.

[25] J.C. Idrobo, J. Rusz, J. Spiegelberg, M.A. McGuire, C.T. Symons, R.R. Vatsavai, C. Cantoni, A.R. Lupini, Detecting magnetic ordering with atomic size electron probes, Adv Struct Chem Imag. 2 (2016) 5. https://doi.org/10.1186/s40679-016-0019-9.

[26] D. Negi, J. Spiegelberg, S. Muto, T. Thersleff, M. Ohtsuka, L. Schönström, K. Tatsumi, J. Rusz, Proposal for Measuring Magnetism with Patterned Apertures in a Transmission Electron Microscope, Phys. Rev. Lett. 122 (2019) 037201. https://doi.org/10.1103/PhysRevLett.122.037201.

[27] H. Ali, D. Negi, T. Warnatz, B. Hjörvarsson, J. Rusz, K. Leifer, Atomic resolution energy-loss magnetic chiral dichroism measurements enabled by patterned apertures, Phys. Rev. Research. 2 (2020) 023330. https://doi.org/10.1103/PhysRevResearch.2.023330.

[28] T. Thersleff, L. Schönström, C.-W. Tai, R. Adam, D.E. Bürgler, C.M. Schneider, S. Muto, J. Rusz, Single-pass STEM-EMCD on a zone axis using a patterned aperture: progress in experimental and data treatment methods, Scientific Reports. 9 (2019) 18170. https://doi.org/10.1038/s41598-019-53373-1.

[29] W. Wulfhekel, J. Kirschner, Spin-Polarized Scanning Tunneling Microscopy of Magnetic Structures and Antiferromagnetic Thin Films, Annual Review of Materials Research. 37 (2007) 69–91. https://doi.org/10.1146/annurev.matsci.37.052506.084342.

[30] P. Fischer, Studying Nanoscale Magnetism and Its Dynamics With Soft X-Ray Microscopy, IEEE Transactions on Magnetics. 44 (2008) 1900–1904. https://doi.org/10.1109/TMAG.2008.924532.

[31] W. Chao, B.D. Harteneck, J.A. Liddle, E.H. Anderson, D.T. Attwood, Soft X-ray microscopy at a spatial resolution better than 15 nm, Nature. 435 (2005) 1210–1213. https://doi.org/10.1038/nature03719.

[32] Linear and Chiral Dichroism in the Electron Microscope, CRC Press. (n.d.). https://www.crcpress.com/Linear-and-Chiral-Dichroism-in-the-Electron-Microscope/Schattschneider/p/book/9789814267489 (accessed January 7, 2019).

[33] W.L. O'Brien, B.P. Tonner, Orbital and spin sum rules in x-ray magnetic circular dichroism, Phys. Rev. B. 50 (1994) 12672–12681. https://doi.org/10.1103/PhysRevB.50.12672.

[34] P. Carra, B.T. Thole, M. Altarelli, X. Wang, X-ray circular dichroism and local magnetic fields, Phys. Rev. Lett. 70 (1993) 694–697. https://doi.org/10.1103/PhysRevLett.70.694.

[35] L. Calmels, F. Houdellier, B. Warot-Fonrose, C. Gatel, M.J. Hÿtch, V. Serin, E. Snoeck, P. Schattschneider, Experimental application of sum rules for electron energy loss magnetic chiral dichroism, Physical Review B. 76 (2007). https://doi.org/10.1103/PhysRevB.76.060409.

[36] J. Rusz, O. Eriksson, P. Novák, P.M. Oppeneer, Sum rules for electron energy loss near edge spectra, Physical Review B. 76 (2007). https://doi.org/10.1103/PhysRevB.76.060408.

[37] H. Lidbaum, J. Rusz, A. Liebig, B. Hjörvarsson, P.M. Oppeneer, E. Coronel, O. Eriksson, K. Leifer, Quantitative Magnetic Information from Reciprocal Space Maps in Transmission Electron Microscopy, Physical Review Letters. 102 (2009). https://doi.org/10.1103/PhysRevLett.102.037201.

[38] J. Rusz, H. Lidbaum, A. Liebig, B. Hjörvarsson, P.M. Oppeneer, S. Rubino, O. Eriksson, K. Leifer,

Quantitative magnetic measurements with transmission electron microscope, Journal of Magnetism and Magnetic Materials. 322 (2010) 1478–1480. https://doi.org/10.1016/j.jmmm.2009.06.032.

[39] S. Muto, K. Tatsumi, J. Rusz, Parameter-free extraction of EMCD from an energy-filtered diffraction datacube using multivariate curve resolution, Ultramicroscopy. 125 (2013) 89–96. https://doi.org/10.1016/j.ultramic.2012.09.008.

[40] Z.Q. Wang, X.Y. Zhong, R. Yu, Z.Y. Cheng, J. Zhu, Quantitative experimental determination of site-specific magnetic structures by transmitted electrons, Nature Communications. 4 (2013) 1395. https://doi.org/10.1038/ncomms2323.

[41] S. Muto, J. Rusz, K. Tatsumi, R. Adam, S. Arai, V. Kocevski, P.M. Oppeneer, D.E. Bürgler, C.M. Schneider, Quantitative characterization of nanoscale polycrystalline magnets with electron magnetic circular dichroism, Nature Communications. 5 (2014). https://doi.org/10.1038/ncomms4138.

[42] T. Thersleff, J. Rusz, S. Rubino, B. Hjörvarsson, Y. Ito, N. J. Zaluzec, K. Leifer, Quantitative analysis of magnetic spin and orbital moments from an oxidized iron (1 1 0) surface using electron magnetic circular dichroism, Scientific Reports. 5 (2015) 13012. https://doi.org/10.1038/srep13012.

[43] X. Zhang, S. Meng, D. Song, Y. Zhang, Z. Yue, V.G. Harris, Epitaxially grown BaM hexaferrite films having uniaxial axis in the film plane for self-biased devices, Scientific Reports. 7 (2017). https://doi.org/10.1038/srep44193.

[44] D. Song, Z. Wang, J. Zhu, Magnetic measurement by electron magnetic circular dichroism in the transmission electron microscope, Ultramicroscopy. 201 (2019) 1–17. https://doi.org/10.1016/j.ultramic.2019.03.008.

[45] C. Donnelly, M. Guizar-Sicairos, V. Scagnoli, S. Gliga, M. Holler, J. Raabe, L.J. Heyderman, Three-dimensional magnetization structures revealed with X-ray vector nanotomography, Nature. 547 (2017) 328–331. https://doi.org/10.1038/nature23006.

[46] C. Donnelly, S. Finizio, S. Gliga, M. Holler, A. Hrabec, M. Odstrčil, S. Mayr, V. Scagnoli, L.J. Heyderman, M. Guizar-Sicairos, J. Raabe, Time-resolved imaging of three-dimensional nanoscale magnetization dynamics, Nature Nanotechnology. 15 (2020) 356–360. https://doi.org/10.1038/s41565-020-0649-x.

[47] J. Rusz, S. Rubino, O. Eriksson, P.M. Oppeneer, K. Leifer, Local electronic structure information contained in energy-filtered diffraction patterns, Physical Review B. 84 (2011). https://doi.org/10.1103/PhysRevB.84.064444.

[48] D. Song, A.H. Tavabi, Z.-A. Li, A. Kovács, J. Rusz, W. Huang, G. Richter, R.E. Dunin-Borkowski, J. Zhu, An in-plane magnetic chiral dichroism approach for measurement of intrinsic magnetic signals using transmitted electrons, Nature Communications. 8 (2017) 15348. https://doi.org/10.1038/ncomms15348.

[49] J. Rusz, P.M. Oppeneer, H. Lidbaum, S. Rubino, K. Leifer, Asymmetry of the two-beam geometry in EMCD experiments, Journal of Microscopy. 237 (2010) 465–468. https://doi.org/10.1111/j.1365-2818.2009.03295.x.

[50] J. Rusz, Role of symmetry in quantitative EMCD experiments, ArXiv:0910.3849 [Cond-Mat]. (2009). http://arxiv.org/abs/0910.3849 (accessed August 24, 2020).

[51] D. Song, J. Rusz, J. Cai, J. Zhu, Detection of electron magnetic circular dichroism signals under zone axial diffraction geometry, Ultramicroscopy. 169 (2016) 44–54.

https://doi.org/10.1016/j.ultramic.2016.07.005.

[52] K. Tatsumi, S. Muto, J. Rusz, T. Kudo, S. Arai, Signal enhancement of electron magnetic circular dichroism by ultra-high-voltage TEM, toward quantitative nano-magnetism measurements, Microscopy. 63 (2014) 243–247. https://doi.org/10.1093/jmicro/dfu002.

[53] P.A. Midgley, R.E. Dunin-Borkowski, Electron tomography and holography in materials science, Nature Materials. 8 (2009) 271–280. https://doi.org/10.1038/nmat2406.

[54] E. Voelkl, D. Tang, Approaching routine $2\pi/1000$ phase resolution for off-axis type holography, Ultramicroscopy. 110 (2010) 447–459. https://doi.org/10.1016/j.ultramic.2009.11.017.

[55] F. Schwarzhuber, P. Melzl, J. Zweck, On the achievable field sensitivity of a segmented annular detector for differential phase contrast measurements, Ultramicroscopy. 177 (2017) 97–105. https://doi.org/10.1016/j.ultramic.2017.02.005.

[56] J. Zweck, F. Schwarzhuber, J. Wild, V. Galioit, On detector linearity and precision of beam shift detection for quantitative differential phase contrast applications, Ultramicroscopy. 168 (2016) 53–64. https://doi.org/10.1016/j.ultramic.2016.05.007.

[57] S. McVitie, M. Cushley, Quantitative Fresnel Lorentz microscopy and the transport of intensity equation, Ultramicroscopy. 106 (2006) 423–431. https://doi.org/10.1016/j.ultramic.2005.12.001.

[58] M. Bonilla, S. Kolekar, Y. Ma, H.C. Diaz, V. Kalappattil, R. Das, T. Eggers, H.R. Gutierrez, M.-H. Phan, M. Batzill, Strong room-temperature ferromagnetism in VSe 2 monolayers on van der Waals substrates, Nature Nanotechnology. 13 (2018) 289. https://doi.org/10.1038/s41565-018-0063-9.

[59] J. Rusz, S. Muto, K. Tatsumi, New algorithm for efficient Bloch-waves calculations of orientation-sensitive ELNES, Ultramicroscopy. 125 (2013) 81–88. https://doi.org/10.1016/j.ultramic.2012.09.009.

[60] J. Rusz, Modified automatic term selection v2: A faster algorithm to calculate inelastic scattering cross-sections, Ultramicroscopy. 177 (2017) 20–25. https://doi.org/10.1016/j.ultramic.2017.01.008.

[61] J. Rusz, S. Bhowmick, M. Eriksson, N. Karlsson, Scattering of electron vortex beams on a magnetic crystal: Towards atomic-resolution magnetic measurements, Phys. Rev. B. 89 (2014) 134428. https://doi.org/10.1103/PhysRevB.89.134428.

[62] N. Shibata, Y. Kohno, A. Nakamura, S. Morishita, T. Seki, A. Kumamoto, H. Sawada, T. Matsumoto, S.D. Findlay, Y. Ikuhara, Atomic resolution electron microscopy in a magnetic field free environment, Nature Communications. 10 (2019) 2308. https://doi.org/10.1038/s41467-019-10281-2.

[63] D. Song, G. Li, J. Cai, J. Zhu, A general way for quantitative magnetic measurement by transmitted electrons, Scientific Reports. 6 (2016). https://doi.org/10.1038/srep18489.

[64] J. Barthel, J. Mayer, J. Rusz, P.-L. Ho, X.Y. Zhong, M. Lentzen, R.E. Dunin-Borkowski, K.W. Urban, H.G. Brown, S.D. Findlay, L.J. Allen, Understanding electron magnetic circular dichroism in a transition potential approach, Phys. Rev. B. 97 (2018) 144103. https://doi.org/10.1103/PhysRevB.97.144103.

[65] J. Rusz, J.C. Idrobo, Aberrated electron probes for magnetic spectroscopy with atomic resolution: Theory and practical aspects, Phys. Rev. B. 93 (2016) 104420. https://doi.org/10.1103/PhysRevB.93.104420.

[66] D.S. Negi, J.C. Idrobo, J. Rusz, Probing the localization of magnetic dichroism by atomic-size astigmatic and vortex electron beams, Scientific Reports. 8 (2018) 4019. https://doi.org/10.1038/s41598-018-22234-8.

[67] D. Negi, P.M. Zeiger, L. Jones, J.-C. Idrobo, P.A. van Aken, J. Rusz, Prospect for detecting magnetism of a single impurity atom using electron magnetic chiral dichroism, Phys. Rev. B. 100 (2019) 104434. https://doi.org/10.1103/PhysRevB.100.104434.

[68] A. Maigné, M. Wolf, Low-dose electron energy-loss spectroscopy using electron counting direct detectors, Microscopy (Oxf). 67 (2018) i86–i97. https://doi.org/10.1093/jmicro/dfx088.

[69] R. Zan, Q.M. Ramasse, R. Jalil, T. Georgiou, U. Bangert, K.S. Novoselov, Control of Radiation Damage in MoS_2 by Graphene Encapsulation, ACS Nano. 7 (2013) 10167–10174. https://doi.org/10.1021/nn4044035.

[70] J.L. Hart, A.C. Lang, A.C. Leff, P. Longo, C. Trevor, R.D. Twesten, M.L. Taheri, Direct Detection Electron Energy-Loss Spectroscopy: A Method to Push the Limits of Resolution and Sensitivity, Scientific Reports. 7 (2017) 8243. https://doi.org/10.1038/s41598-017-07709-4.

[71] B. Plotkin-Swing, G.J. Corbin, S. De Carlo, N. Dellby, C. Hoermann, M.V. Hoffman, T.C. Lovejoy, C.E. Meyer, A. Mittelberger, R. Pantelic, L. Piazza, O.L. Krivanek, Hybrid pixel direct detector for electron energy loss spectroscopy, Ultramicroscopy. (2020) 113067. https://doi.org/10.1016/j.ultramic.2020.113067.

[72] J. Spiegelberg, D. Song, R.E. Dunin-Borkowski, J. Zhu, J. Rusz, Blind identification of magnetic signals in electron magnetic chiral dichroism using independent component analysis, Ultramicroscopy 195 (2018) 129–135. https://doi.org/10.1016/j.ultramic.2018.08.021.